IMaging-based CUSTOMised EYE diagnostics

Project ID: 779960

Funded under: H2020-EU.2.1.1. - INDUSTRIAL LEADERSHIP - Leadership in enabling and industrial technologies - Information and Communication Technologies (ICT)

Deliverable D.6.2
Report on diagnostic value of imaging tool for keratoconus and IOP-related glaucoma

Document control information

Title	Report on diagnostic value of imaging tool for keratoconus and IOP-related glaucoma
Contributing partners	CSIC, ULIV
Type	Report
Dissemination level	❒ **CO** Confidential, only for members of the consortium (including the Commission Services) ❒ **RE** Restricted to a group specified by the consortium (including the Commission Services) ❒ **PP** Restricted to other programme participants (including the Commission Services) ☒ **PU** Public
Status	❒ Draft ☒ WP Manager accepted ☒ Co-ordinator accepted
Due date	30/11/2022
Delivery date	15/12/2022
Action requested	❒ to be revised by Partners involved in the preparation of the deliverable ❒ to be reviewed by applicable IMCUSTOMEYE Partners ❒ for approval of the WP Manager ❒ for approval of the Project Coordinator

Revision history

Version	Date	Author	Comment
1.0	30.11.2022	Judith Birkenfeld	Initial version
2.0	09.12.2022	Ashkan Eliasy	Methods, numerical models; Results, paragraph on numerical models
3.0	11.12.2022	Judith Birkenfeld	Method, numerical models; Results, numerical models
4.0	14.12.2022	Fernando Zvietcovich	Ultrasound modules and results in Sections: Introduction, Method, and Results.
5.0	15.12.2022	Judith BIrkenfeld	Final version for review
6.0	25.12.2022	Susana Marcos	Final version

Table of contents

1   Summary

We report the results from two patient studies with keratoconus patients, using (1) the *air-puff excitation module*, as presented in deliverable 6.1, (2) an alternative excitation module based on elastography, *confocal air-coupled ultrasonic OCE.* Both excitation modules are coupled to the CSIC-based swept source OCT device, presented in deliverable 6.1. This deliverable presents approaches to analyze newly introduced cross-meridian air-puff deformation imaging, it suggests novel biomarkers based on elastography, and it shows the capability of the software module ImSoftDiagnose for biomechanical analysis and corneal mapping. The results are promising and show the advantages of the novel excitation approaches, and their value in supporting the early diagnosis of keratoconus in a clinical setting.

2   Introduction

Accurate estimation of the cornea's material stiffness is very important for corneal diagnostics and treatment planning and guidance. We have introduced different modules for corneal excitation to investigate corneal biomechanical behavior in KC patients and a control group. The results from the air-puff excitation module was combined with Hyperelastic-viscoelastic 3D numerical models that were built using subject-specific tomographic data, and prior knowledge of the cornea's and sclera's material properties (deliverable 2.2 and 6.1). The corneal material stiffness was estimated after an inverse solution algorithm, similar to those utilized previously [1, 2], found the material stiffness that minimized the root-mean-square (rms) error between the numerical and experimental corneal deformation spatial-temporal profile. The ultrasound excitation module was used to produce mechanical wave propagation in human corneas that were capture by the CSIC-based swept source OCT. Wave speed and corneal thickness were calculated in 16 semi-meridians of 60 healthy corneas of a control group in order to create the beaseline of mormal biomechanics of two propoased biomarkers: speed-thickness index and the spatial anistropy of wave speed. The system and method have been tested on 16 subclinical keratoconus corneas, 13 corneas with keratoconus (level I), and 14 corneas with intracorneal ring segments *in vivo*.

3   Material and methods

1) AIR-PUFF DEFORMATION IMAGING
Figure 1 shows a schematic of the corneal cross-meridian air-puff deformation OCT that was used to image air-puff induced deformation on patients and healthy subjects. The system was presented in [3], deliverable 2.2, and deliverable 6.1. It allows for the first time to monitor deformation on two corneal meridians, which are then processed to segment and extract the corneal deformation profile over time as referenced to a coordinate system centered in the corneal apex before deformation in the x, y lateral coordinates and at the air-puff outlet position in the z axial coordinate.
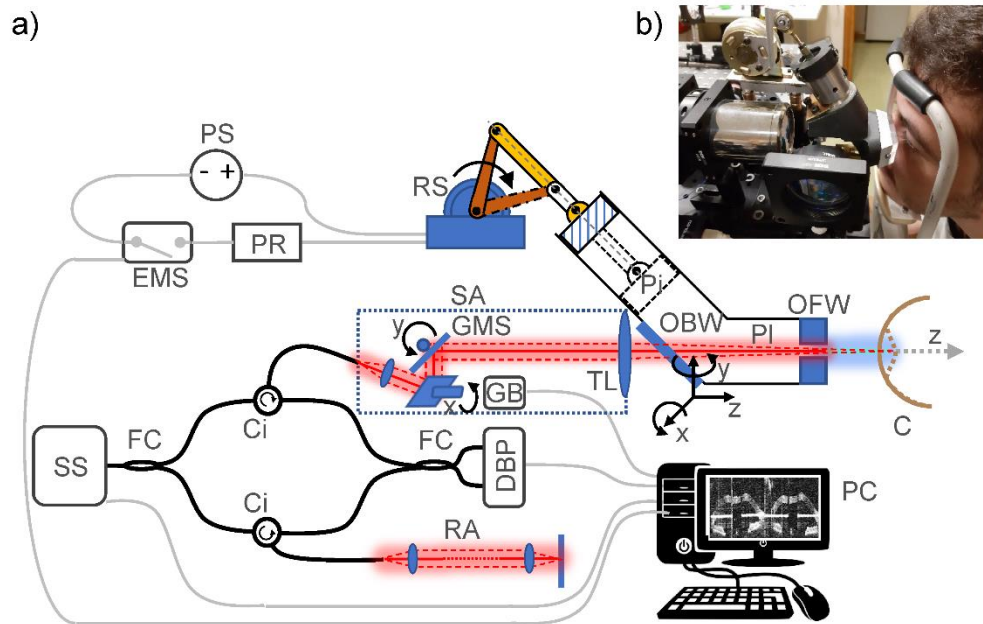
Figure 1: Cross-meridian air-puff deformation OCT, measuring corneal deformation over two orthogonal corneal meridians.

To accurately segment and quantify the corneal deformation in time from the captured OCT images, an algorithm based on the concepts of snakes and deformable models was implemented [4, 5]. This algorithm allowed to automatically (or semi-automatically) segment the anterior corneal surface and its deformation from OCT images in different meridians by adaptively following the deformation in time. Figure 2 shows the horizontal (left) and vertical (right) meridian of a segmented human cornea *in vivo*.
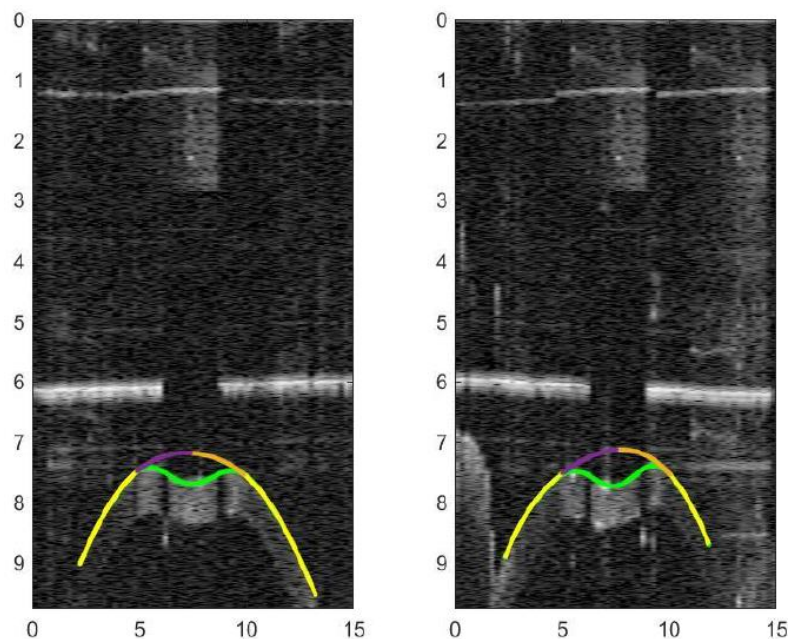
Figure 2: A snake algorithm segmented the corneal surfaces in horizontal (left) and vertical (right) meridian by adaptively following the deformation in time.

After segmentation, i.e., quantification of the deformation, three cross-meridian deformation parameters were investigated, a) the *peak distance* for horizontal and vertical meridian, that is, the distance between the two highest points of the cornea at maximum deformation (fig. 3 a), b) the *deformation amplitude (DA)* ratio (describing the *shape* of corneal deformation), defined as the ratio between maximum deformation amplitude at the apex and the average of three deformation amplitudes at three distances from the apexfor both, hotizontal and vertical meridian (see fig. 3 b), and c) the *asymmetry ratio* Asymmetry Ratio (AR, describing possible deformation *asymmetries*), defined as the ratio between nasal/temporal (horizontal) and superior/inferior (vertical) deformation amplitudes at three distances from the corneal apex (fig. 3 c).
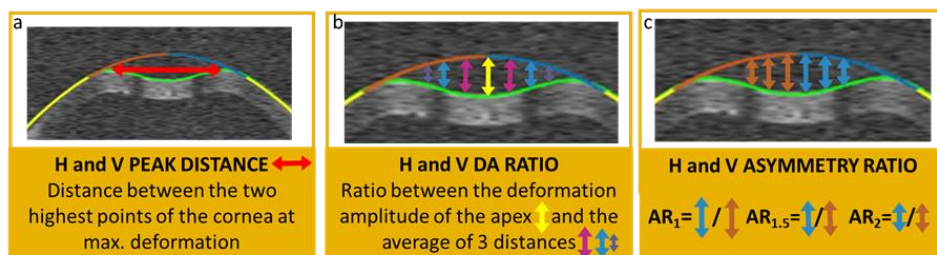

Figure 3: Investigated deformation parameters at maximum corneal deformation, a) peak distance, b) deformation amplitude (DA) ratio and c) asymmetry ratio in horizontal and vertical meridian.

A mixed model analysis was used to globally determine the significance of the investigated parameters between a) subject groups, b) horizontal and vertical meridian, c) measurement distance from corneal apex. ANOVA multiple comparison analysis and post-hoc tests were applied to find significant differences between groups for each deformation parameter. The homogeneity of variances was tested by Levene's test. Tests were considered to be significant at $p < 0.05$ level.

2) NUMERICAL MODELS

The present study relied on numerical models simulating the behaviour of the eye globe under the effects of IOP and external air pressure. The finite element software package ABAQUS 6.13 (Dassault Syst.mes Simulia Corp., Rhode Island, USA) was used to simulate the Corvis ST testing procedure on models of the human eye. The models included the eye's outer tunic (cornea and sclera) and internal fluids (aqueous and vitreous), but excluded other components of the orbit. Following a mesh density study, each model was built with 800 15-noded continuum elements (C3D15H) connected by 3606 nodes and organised in one layer, 10 cornea rings and 10 sclera rings, Figure 4 [6, 7]. The models were generated using a bespoke ocular model generator software developed in house. The optic nerve head was omitted as its inclusion was found in the study to have a negligible effect on corneal deformation under both IOP and external air pressure.
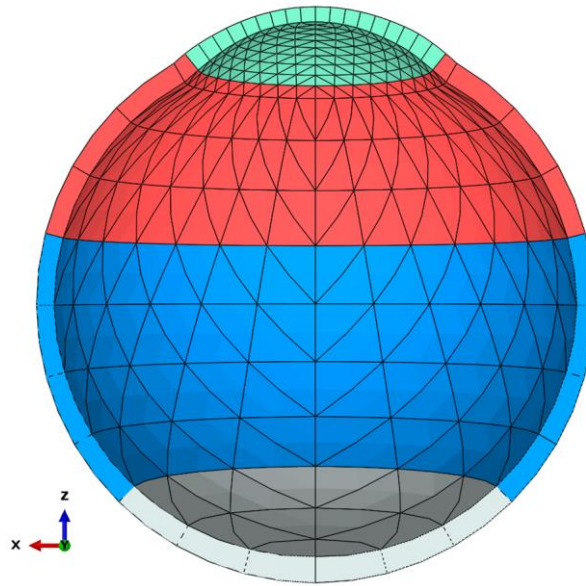
Figure 4: A typical cross-section of the full eye FE model, where colours represent different material properties.

The models adopted the geometric features of the ocular globe reported in earlier studies. The corneal shape factor was set at 0.82, the limbal radius at 5.85 mm and the scleral radius at 11.5 mm. The peripheral corneal thickness (PCT) at the edge of the limbus was assumed to be 150 μm more than CCT, while the sclera equatorial thickness was set at 0.80 PCT and the posterior pole thickness at 1.20 PCT [8, 9, 10].

IOP was defined using a surface-based fluid cavity, the pressure of which can be controlled. The cavity was assumed to be filled with an incompressible fluid with a density of 1,000 kg/m^3 to represent the vitreous and aqueous humour [11]. In all models, rigid-body motion was prevented by restraining the equator nodes in the anterior-posterior direction, and the posterior pole in both the superior-inferior and temporal-nasal directions. Inflation was followed by the application of IOP and then the Corvis ST air pressure. While IOP was applied as a uniformly-distributed internal cavity pressure, the spatial and temporal distribution of the Corvis ST pressure on the corneal surface followed the results obtained from experimental study through.

To measure the air-puff pressure, two different power resistors (4.7 and 33 Ω) which provided a steady-state voltage drop over the solenoid of 41.75 V and 23.30 V, respectively, when connected to the 48 V DC power supply were used (ref). Both configurations were tested with the air-puff outlet at distances to the sensor of 11 mm (standard), 9 mm and 13 mm (for the higher voltage). Fig. xx shows the apical temporal pressure profile for all three distances from the air-puff outlet to the corneal apex, for the higher voltage configuration. The maximum pressure increased by 38% going from a distance of 13 mm to 9 mm. Figures 5(c) and 5(d) present the spatial pressure profile at the time of maximum apical pressure for the low and high solenoid voltage configuration, respectively. For herein presented work, the high voltage configuration was used.
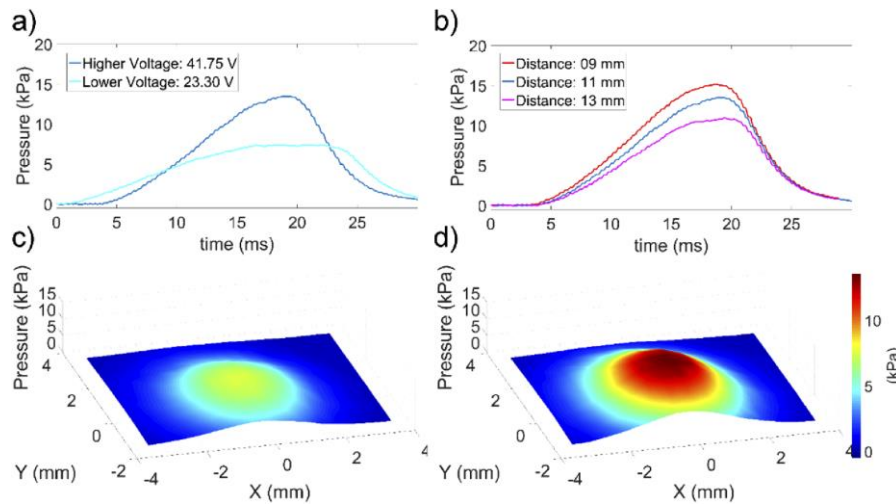
Figure 5: Air-puff characterization for different solenoid voltages and different distances of the air-puff outlet to the sensor. Taken from [3].

A previously published approach was used to identify the location of pathology on patient's cornea [12]. The model's corneal geometry and thickness were customized according to patient topography and tomography data captured using Pentacam. In the event pathology existed, the cornea would adapt unique material properties for that specific area, different from the rest of the cornea. Finally, an inverse analysis approach was adapted to optimize the material properties of the cornea and pathology area. The objective function was to minimize the root mean square of the error between the model deformation and the actual deformation of the cornea under air puff that was captured from the patient.

3) ULTRASOUND EXCITATION MODULE

A 500 kHz ultrasonic air-coupled transducer co-focused with a swept-source optical coherence tomography system reported in [13] was used to generate quasi-harmonic mechanical perturbation at the corneal apex as shown in Figure 6. The transducer possesses a 15 mm diameter aperture to allow for OCT imaging while ultrasonic acoustic pressure is being focus at a spot diameter of <1mm at the apex of the cornea. The acoustic excitation produces nanometer displacement waves propagating outwards in the corneal surface during a 1ms time window.
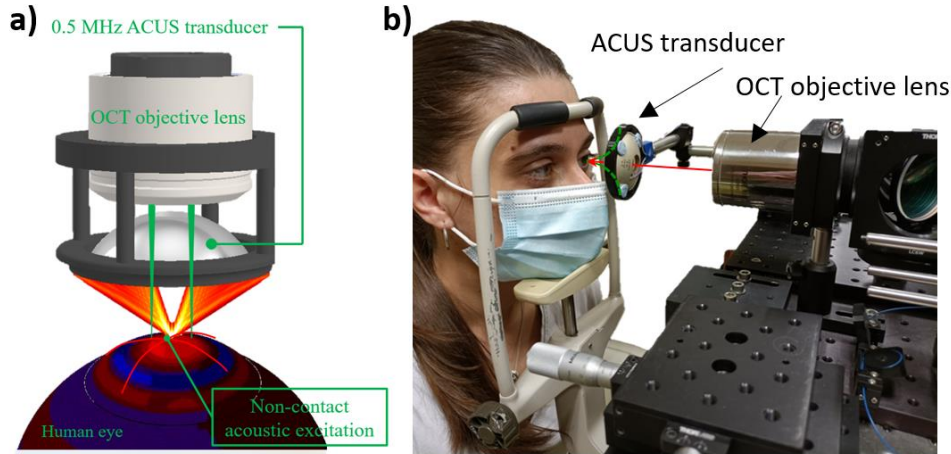
Figure 6: Ultrasonic excitation module setup. In (a), the 500 kHz ultrasonic air-coupled transducer is co-focused with the sample arm of the swept-source OCT system reported in [13] in order to produce Lamb wave propagation in the cornea. In (b), the real distribution of the ultrasonic transducer, OCT objective lens with respect to the patient cornea is shown.

Lamb wave propagation speed and average thickness were measured within 16 corneal semi-meridians covering 360 degrees during 1s of total acquisition. The phase-sensitive information of the OCT acquisition was used to generated sequences of displacement images depicting wave propagation, while the structural OCT images were utilized for the calculation of average corneal thickness per semi-meridian (Figure 7a). Subsequently, spatio-temporal maps of wave propagation were calculated from the displacement sequences along the segmented corneal surface (Figure 7b). Lamb wave propagation speed were estimated at the mechanical frequency of 3500 Hz from speed dispersion plots obtained using the 2D Fourier transform of the spatio-temporal maps as shown in Figure 7c. Finally, this process is repeated in all the corneal semi-meridians in order to create a speed map of the cornea (Figure X2d).
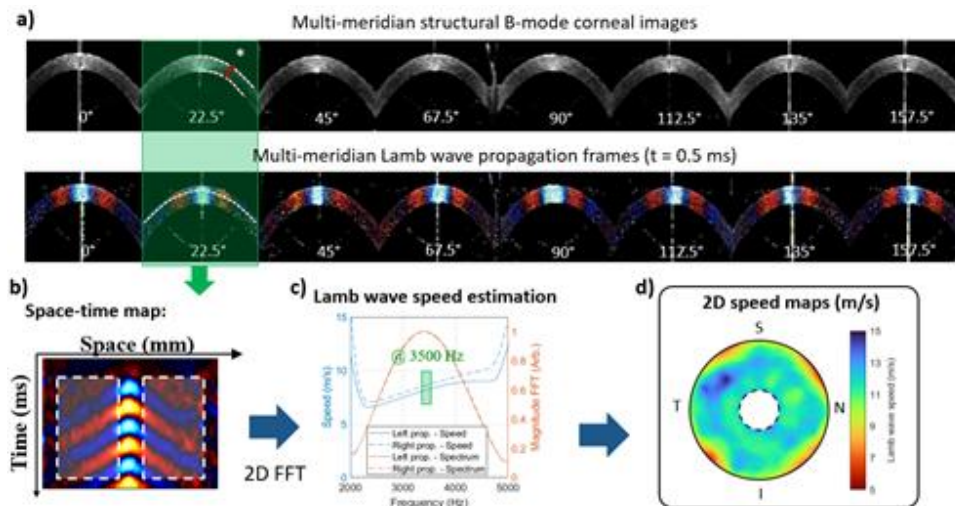

Figure 7: Wave propagation processing approach. In (a), structural (B-mode) and motion images (wave propagation) of the cornea in 16 semi-meridians are show. (b) Spatio-temporal maps are obtained along the propagation path of the wave in the corneal surface. (c) Lamb wave speed estimation at 3500 Hz based on speed dispersion maps obtained after applying the 2D Fourier Transform to (b). In (d), 2D speed maps of the cornea are obtained after estimating (c) in all corneal semi-meridians.

Measurements in 30 human healthy subjects (control group: CG, N = 60 corneas; age: 20-50 years old) defined a baseline of normal biomechanics in two biomarkers: spatial anisotropy of wave speed (SAWS) and the Speed-Thickness Index (STI). In one hand, the SAWS is calculated from the meridionally dependent wave speed map and provides information of the relative symmetry of the cornea biomechanics along its whole extension. The SAWS was characterized using the normalized fractional anisotropy metric that takes the value of SAWS = 0 for perfect isotropy, and SAWS = 1 for complete anisotropy. We found an average SAWS = 0.207 in control corneas. On the other hand, the STI was defined as the speed deviation of each corneal semi-meridian compared to the baseline speed measured in the control corneas. Then, a STI > 0 m/s signifies a normal or stiffer cornea; while a STI < 0 m/s suggest a biomechanically abnormal or softer cornea. The STI can be shown as a map in the whole extension of the cornea to localize regions with abnormal elasticity. Figure 8 shows the developed software showing the STI maps, speed polar plots, SAWS, and speed-thickness plots of a control patient (N = corneas) with respect to the database of 60 control corneas. In the STI maps, the cold and hot color pallet depicts normal and abnormal corneal biomechanics.
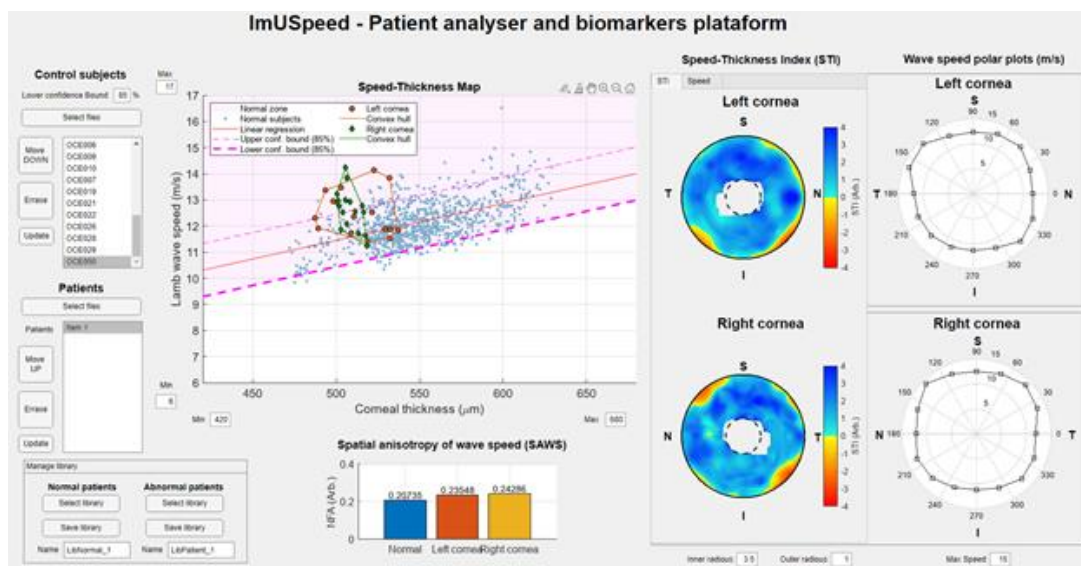

Figure 8: Software platform showing the analysis of the Speed-Thickness Index (STI) and Spatial Anisotropy of Wave Speed (SAWS) biomarkers of a control patient (both corneas) in comparison to the baseline calculated from 60 control corneas.

4) PATIENT STUDY

The above-described excitation modules *Air-Puff* (1) and *Ultrasound* (2) have been used in two patient studies, that were executed in collaboration with the Fundación Jimenez Diaz (FJD) and the Fundacion Fernandez Vega (FFV). Keratoconus patients included patients with keratoconus stage I, II; form fruste (FF), and subclinical keratoconus.

All recruited patients were first diagnosed at the collaborating hospitals and then measured at IO-CSIC using the ImTOPScanner. All patient were additionally measured with commercial instruments (Corvis, Pentacam; Oculus, Germany). One visit to the IO-CSIC was required for all patients. Figure 9 gives an overview of patient and data flow.
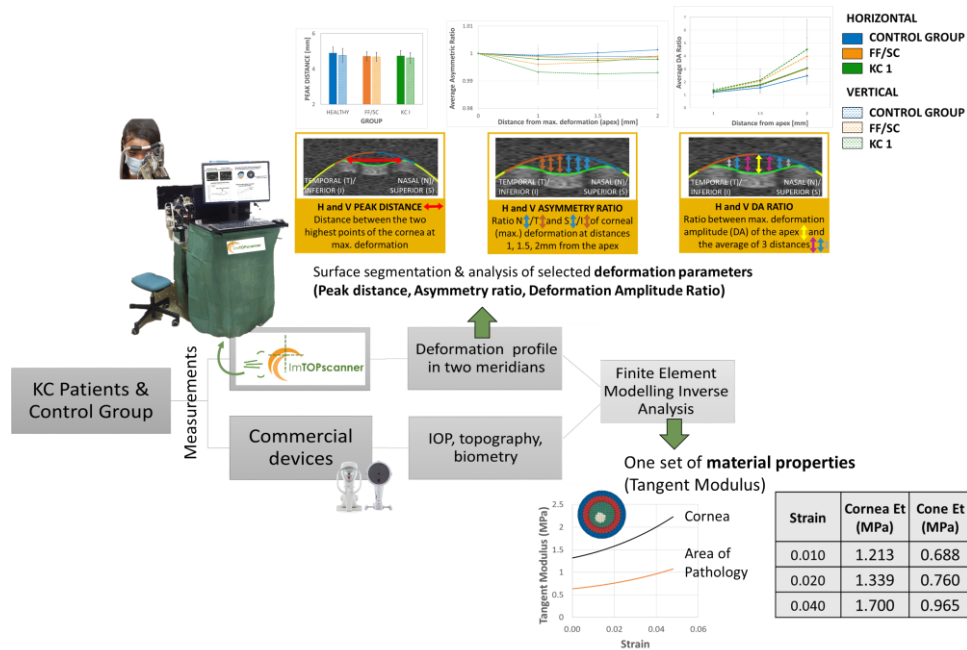

Figure 9: Overview of measurements and data handling, and data analysis at IO-CSIC, in collaboration with University of Liverpool.

Because of the restrictions due to COVID-19, mainly keratoconus patients have been recruited. (1 session per patient). Healthy subjects were added to the study as comparison group. Measurements took less than 100 ms to acquire for a single air-puff release and 1s for an Ultrasound measurement. 3-5 measurements were acquired per patient for averaging purposes. For the patient study with the Ultrasound module, a total of 30 control patients (N = 60 healthy corneas) and 25 keratoconus patients where measured. Moreover, the keratoconus patient study was divided in 16 subclinical/ form fruste (SK/FF) keratoconus corneas, 13 corneas with keratoconus level I (KC 1), and, additionally, 14 corneas with keratoconus level I that were treated with intracorneal ring segments (KC 1 + ICRS). All human experiments have been conducted in accordance with the tenets of the Declaration of Helsinki and approved by the institutional research ethics committee and written and informed consent has been obtained.

4   Results

We present the following results:

1) Novel parameters from cross-meridian air-puff deformation imaging combined with the software modules (Imsoftdiagnose) developed in Workpackage 6.1 to estimate corneal biomechanical properties in partients.

2) Novel biomarkers based on the meridional-dependent corneal wavespeed and its spatial anisotropy, calculated from occurring corneal surface waves during excitation.

4.1 Cross-meridian air-puff deformation imaging combined with Imsoftdiagnose

Novel parameters from cross-meridian deformation imaging: Corneal deformation images were obtained, as described in deliverable 6.1.,
Figure 10 shows and compares the averaged results of the peak distance for three different groups, 1) healthy, 2) Form Fruste (FF)/subclinical (SC), and 3) KC 1. Mixed model analysis showed a significant difference (p<0.05) between all subject groups and between the horizontal and the vertical meridian.
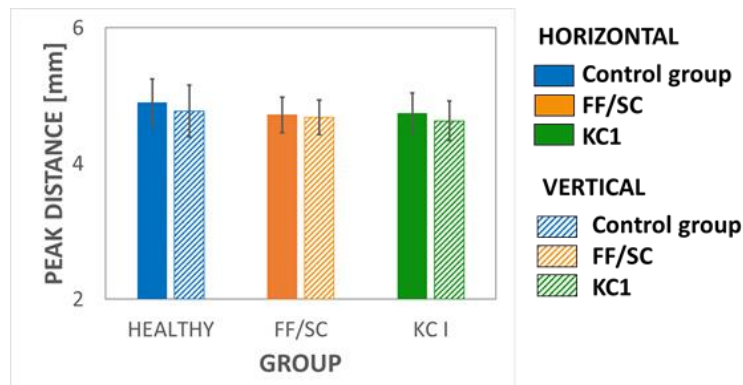

Figure 10: Peak distance at maximum deforation for different patient groups (orange, blue) and the control group (green) for horizontal (solid) and vertical (dashed) meridian.

The DA ratio increased for all groups compared to the control group, but more so in the newly introduced vertical meridian, indicating a change in the deformation shape, mainly on the vertical meridian. Figure 11 shows an average of patients from the control group, FF/SC, and KC I patients. Here, the DA ratio increased up to 0.94±0.49 and 1.48±1.39 for FF/SG and KC I patients, respectively at a distance of 2mm from the corneal apex. Significant differences (p<0.05) between all groups were found for both meridians.
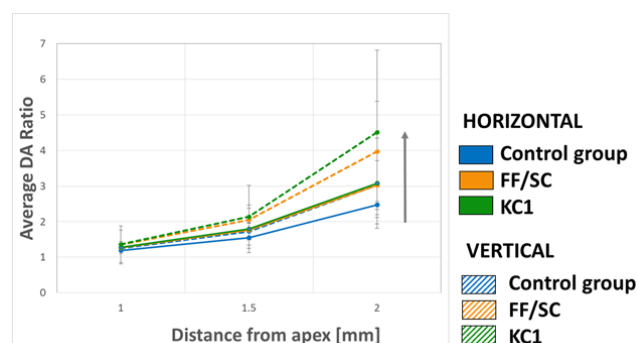

Figure 11: DA ratio increased for all groups compared to CG, more so in V meridian (up to 0.94±0.49 and 1.48±1.39 for FF/SG and KC I patients, respectively at 2mm). Significant differences (p<.05) between all groups were found for both meridians.

Figure 12 visualizes the deformation asymmetries at maximum deformation, measured at three distances from the corneal apex, at four locations of the cornea (superior, inferior, nasal, temporal), for all patient groups (orange, green), and the control group (blue). Shown is the percent difference in deformation amplitude when comparing the maximum deformation at the corneal apex with the maximum deformation at superior, inferior, nasal, and temporal corneal locations,

at 3 distances from the corneal apex. The results of each group are rescaled by dividing all values by the max. deformation at the corneal apex (dark gray line, 100% deformation). It is visually clear that the deformation at the superior location decreases for FF/SC and KC I in comparison to the healthy control group, suggesting mainly a asymmetric deformation behavior in the vertical meridian.

Figure 12: Percent difference in deformation amplitude when comparing max. deformation at the corneal apex with max. deformation at superior, inferior, nasal, and temporal corneal locations, at 3 distances from the corneal apex. Blue-control group, orange-FF/SC group, green-KC1

Figure 13 aims to quantify this asymmetric deformation behavior. Shown here is the average asymmetry ratio for all subjects at all distances from the corneal apex. Generally speaking, the closer the asymmetry ratio AR is to 1, the more symmetric is the deformation. Figure 13 shows that in the vertical meridian the AR decreased up to 0.30 ±0.05% for FF/SC (1mm) and up to 0.64 ±0.21% for KC I (1.5mm) when compared to the control group. CG. Significant differences ($p < 0.05$) in AR between all groups were found only for the vertical meridian, which supports the hypothesis that localized biomechanical changes as they typically occur in KC patients in the lower periphery of the cornea (on the vertical meridian) result in asymmetric deformation, but only on the "affected" meridian.
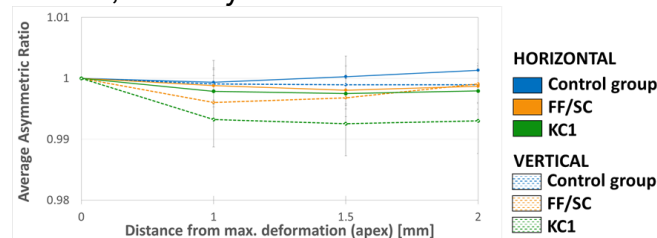

Figure 13: Asymmetry Ratio (AR) for control group (blue), FF/SC patients (orange), and KC patients (green). Significant differences ($p < 0.05$) in AR between groups were only found for the vertical meridian.

Above results on selected deformation parameters indicate that the analysis of deformation parameters alone may give an important diagnostic value to current diagnostic procedures for early KC detection, since they give subtle information about changing deformation shape and asymmetry of KC eyes, hence they may indicate a direction of biomechanical changes. Additionally, the use of ratios makes the use of deformation parameters more convenient, since they are not dependent on the intraocular pressure of the eye.

To retrieve actual biomechanical parameters, the above-described deformation data was additionally used as input data for Finite Element (FE) modeling inverse analysis. In collaboration with imcustomeye partner University of Liverpool, patient-specific FE models were generated, based on corneal geometry,

intraocular pressure, and age-related scleral material properties. For KC eyes, an algorithm detected the area of pathology and allocated a separate material for the affected region. Through an inverse analysis procedure, corneal material stiffness for second-order Ogden material model was estimated for each patient. Ogden adapts two material parameters, one which defines the nonlinearity of the material and the other that defines the stiffness. To enable comparison between different eyes, the parameter that defines non-linearity was fixed to a constant value of 20. The stiffness value was then compared between patients and between the healthy and diseased parts of the same cornea.

Figure 14 shows an example of the numerical eye model for a healthy (Fig. 14 a, left column) and a KC1 human eye (Fig. 14 a, right column) numerical model construction and the associated deformation during the air-puff event (Fig. 14, last row).
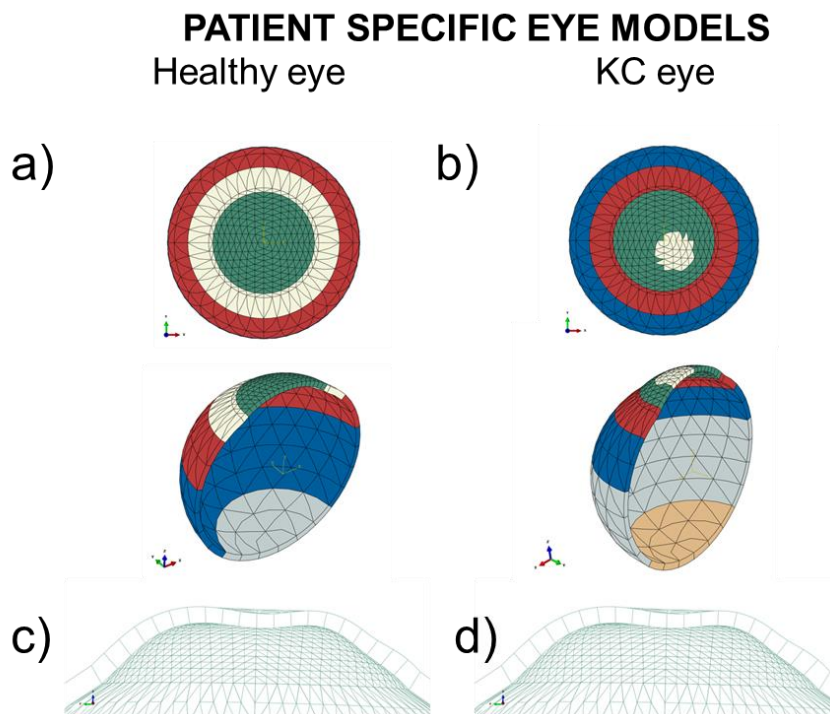

Figure 14: Patient-specific numerical eye models for a healthy (a) and a KC1 (b) human eye, and the associated deformation behavior (c) and d) for healthy and KC eye, respectively).

When the root-mean-square error between the numerical and experimental corneal deformation spatial-temporal profiles was less than 500 μm, the inverse solver estimated the tangent modulus for the eyes' materials at 1%, 2%, and 4% strain. Figure 15 shows example results of the tangent modulus at different strains of one healthy (a), one form fruste (b), and one KC 1 (c) eye. At 4% strain, the tangent modulus was 1.68 MPa for the healthy eye. For the FF/SC and the KC 1 eye, in the area of pathology the tangent modulus lowered to 1.32 MPa and 0.97 MPa, respectively, indicating a softer area of the cornea.
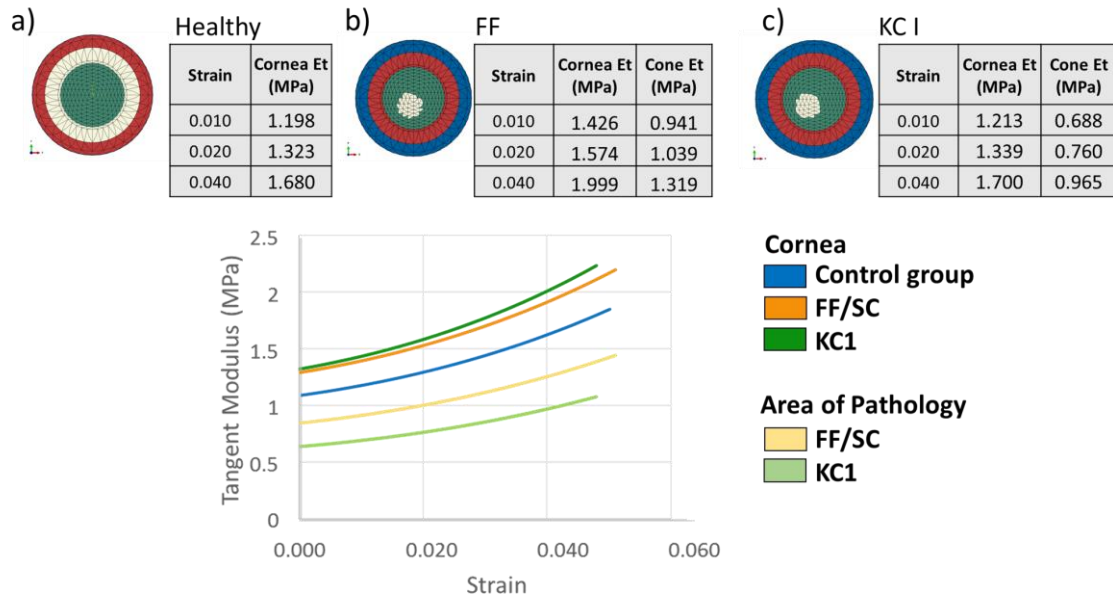
Healthy	
Strain	Cornea Et (MPa)
0.010	1.198
0.020	1.323
0.040	1.680

FF		
Strain	Cornea Et (MPa)	Cone Et (MPa)
0.010	1.426	0.941
0.020	1.574	1.039
0.040	1.999	1.319

KC I		
Strain	Cornea Et (MPa)	Cone Et (MPa)
0.010	1.213	0.688
0.020	1.339	0.760
0.040	1.700	0.965

Figure 15: Example results of the tangent modulus at different strains of one healthy (a), one form fruste (b), and one KC 1 (c) eye.

Figure 16 shows the average of collected data of all subject groups. For KC eyes, where an area of pathology could be detected, the tangent modulus was lower in the area of pathology for all subjects. At 2% strain the area of pathology in KC eyes showed around 30% stiffness reduction compared to healthy areas.
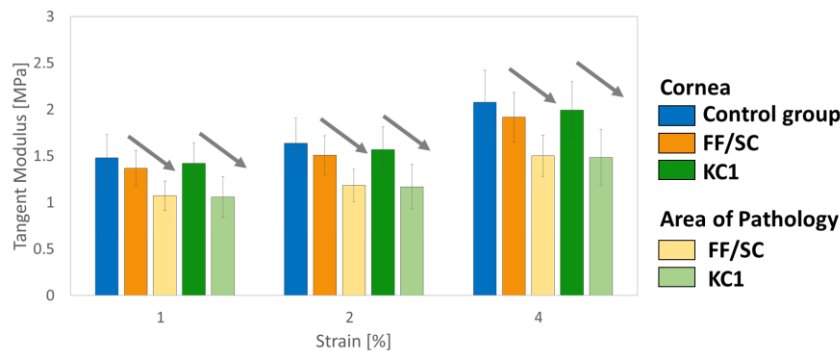

Figure 16: The area of pathology shows a lower tangent modulus for all patients (shown is the average of all eyes/groups).

4.2 Ultrasound excitation module:

Biomarker 1 - Speed Thickness Index: Based on the speed and corneal thickness measurements of the 16 corneal semi-meridians of all the control patients, a linear correlation between wave speed and thickness was found (RMSE = 0.738, $p <$ 0.001, N = 960 speed-thickness pairs) as shown in Figure 17a. After compensating for the physical dependence of Lamb wave speed and thickness, we found that a thicker cornea is stiffer than a thin one. A 90% confidence level was used as a baseline metric to separate normal (stiffer) from abnormal (softer) corneal elasticity. In Figure 17a, we show the speed-thickness pairs of corneas

coming from a patient with diagnosed with KC 1 (left cornea) in one eye, and subclinical keratoconus in the contralateral eye (right cornea). It is evident that, in the case of subclinical keratoconus, at least two semi-meridians are in the pathological region; while for the KC 1 case, 9 out of 16 semi-meridians are compromised. Moreover, with respect to the baseline, the STI can be calculated as map.
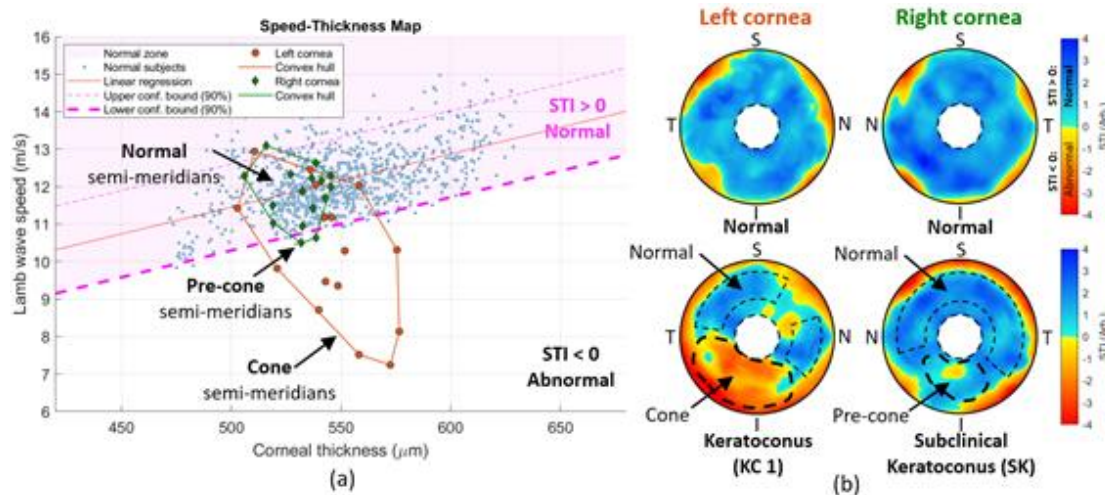

Figure 17: (a) Space-Time Map showing speed and thickness semi-meridians of a KC 1 (left) and SC (right) corneas of one patient. The lower 90% confidence bound separates normal from abnormal biomechanics. (b) STI maps of the right and left corneas of a normal control subject (top row), and keratoconus patient (bottom row) shown in (a). STI: Speed-Thickness Index; T: temporal, N: nasal, S: superior, I: inferior.

In Figure 17b, we show STI maps of a control patient (top row) versus the patient shown in Figure 17a (bottom row). It is clear that the area of abnormal elasticity (depicted with hot color platter, also called as cone) is located in the temporal-inferior region of the cornea and it has a much larger area than the abnormal region in the subclinical cornea (also called as pre-cone).

Biomarker 2 - Spatial Anisotropy of Wave Speed: The relative symmetry of speed measurements of the 16 corneal semi-meridians of all the control patients was found to be SAWS = 0.207 ± 0.026 (N = 960 speed-thickness pairs). In Figure 18a we show the speed polar plots along with the STI maps of a patient with diagnosed with KC 1 (left cornea) in one eye, and subclinical keratoconus in the contralateral eye (right cornea). The calculation of the SAWS and the comparison with the average of controls was conducted for a control patient (both corneas) and the patient showed in Figure X5a (bottom row) as shown in Figures 18b and 18c respectively. Even though the anisotropy of the SC/FF cornea is not as evident as the KC 1 case in the polar plots, the SAWS biomarkers is able to distinguish it with respect to the average SAWS for control corneas.
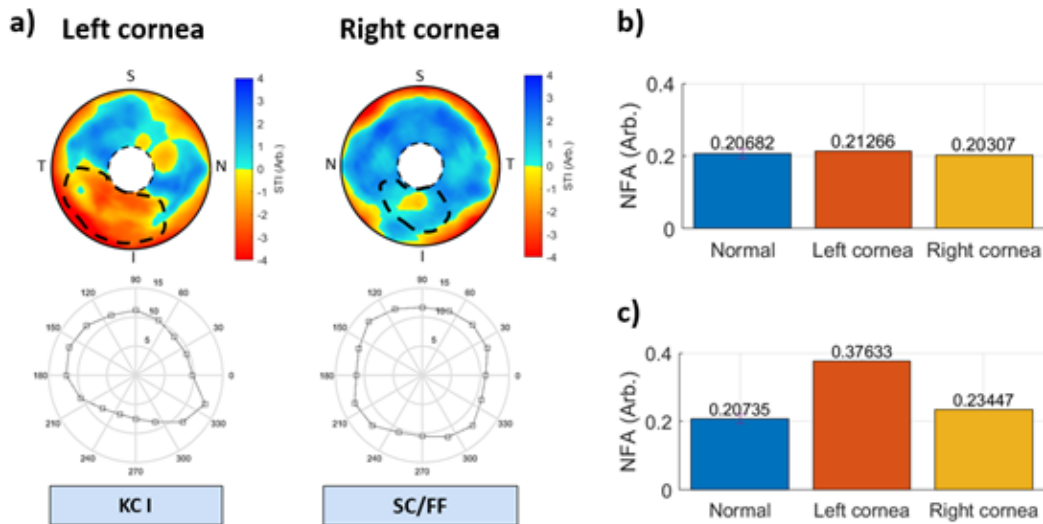
Figure 18: (a) STI maps along with speed polar plots showing of a KC 1 (left) and SC/FF (right) corneas of one patient. SAWS biomarker expressed in terms of Normalized Fractional Anisotropy (NSF) of a (b) control patient and (c) the keratoconus patient shown in (a). In both cases, the SAWS is compared with the average NFA of all the control patients. STI: Speed-Thickness Index; T: temporal, N: nasal, S: superior, I: inferior.

Statistical analysis of all patient measurements: We calculated STI maps of corneas and found abnormal elasticity (STI < 0) in an average of 10 out of 16 meridians in KC 1 corneas (average negative STI = -0.864 ± 0.271, N = 13 corneas), in 5 out of 16 meridians in SC/FF corneas (average negative STI = -0.305 ± 0.229, N = 16), and in 12 out of 16 meridians in KC 1 + ICRS corneas (average negative STI = -1.464 ± 0.311, N = 14) compared to the control group (average negative STI = -0.006 ± 0.005, N = 60) as shown in Figure 19a. Moreover, we found that the STI was statistically significantly higher in SC/FF ($p < 0.001$), KC 1 ($p < 0.001$), and KC1 + ICRS ($p < 0.001$) corneas when compared to the controls. Finally, we found that SAWS was statistically significantly higher in SC/FF (0.2738, $p < 0.001$), KC 1 (0.337, $p < 0.001$), and KC1 + ICRS (0.357, $p < 0.001$) corneas when compared to the control group as shown in Figure 19b.
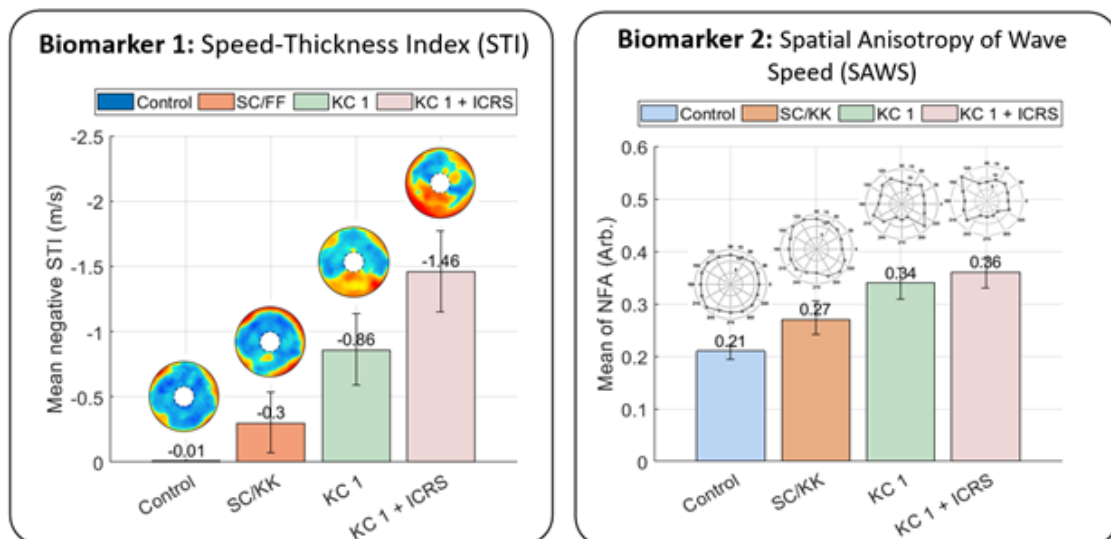

Figure 19: (a) Mean negative STI of corneas coming from the control group, and the SC/FF, KC 1 and KC 1 + ICRS patients. (b) Mean of the normalized fractional anisotropy of the wave speed in corneas coming from the control group, SC/FF, KC 1, and KC 1 + ICRS patients.

5   Conclusions

- Cross-meridian air-puff deformation showed that the additional vertical meridian allows more significant use of deformation parameters as biomarkers of biomechanical changes
- The concept of cross-meridian deformation imaging enables the introduction of deformation *ratios*, which are IOP independent parameters.
- Previously developed hyperelastic-viscoelastic-anisotropic 3D numerical models of the eye were successfully utilized in an inverse solver for the corneal stiffness.
- Cornea models were patient-specific and they adapted different material properties in the pathology area that was detected automatically
- Both biomarkers proposed with the ultrasound module: STI and SAWS can differentiate corneas with subclinical keratoconus from the ones with keratoconus level 1 (with and without ICRS) and the control group.
- Keratoconus corneas with ICRS tend to have less rigidity than KC 1 corneas; however, they maintain the similar levels of mechanical anisotropy.
- Both biomarkers: STI and SAWS could be used, individually or in conjunction, as potential biomarkers to identify "at-risk" corneas before changes in topography and pachymetry become evident in keratoconus.
- Future work will follow sensitivity and specificity studies of proposed KC biomarkers on a larger sample of keratoconus (and their contralateral) eyes.

6   References

1.   A. Elsheikh, B. Geraghty, P. Rama, M. Campanelli, and K. M. Meek, "Characterization of age-related variation in corneal biomechanical properties," J R Soc Interface 7, 1475-1485 (2010).

2.   B. Geraghty, C. Whitford, C. Boote, R. Akhtar, and A. Elsheikh, "Age-Related Variation in the Biomechanical and Structural Properties of the Corneo-Scleral Tunic," in Mechanical Properties of Aging Soft Tissues, B. Derby and R. Akhtar, eds. (Springer International Publishing, Cham, 2015), pp. 207-235.

3.   A. Curatolo, J. S. Birkenfeld, E. Martinez-Enriquez, J. A. Germann, J. Palací, D. Pascual, G. Muralidharan, A. Eliasy, A. Abass, J. Solarski, K. Karnowski, M. Wojtkowski, A. Elsheikh, and S. Marcos, "Multi-meridian corneal imaging of air puff induced deformation for improved detection of biomechanical abnormalities," Biomed. Opt. Express (submitted) (2020).

4.   M. Kass, A. Witkin, and D. Terzopoulos, "Snakes: Active contour models," International Journal of Computer Vision, vol. 1, pp. 321-331, 1988/01/01 1988.

5.   T. F. Cootes, C. J. Taylor, D. H. Cooper, and J. Graham, "Active Shape Models-Their Training and Application," Computer Vision and

Image Understanding, vol. 61, pp. 38-59, 1995/01/01/ 1995.

6. Eliasy A. In vivo Measurement of Corneal Stiffness and Intraocular Pressure to Enable Personalised Disease Management and Treatment. Liverpool, UK: University of Liverpool; [Doctoral thesis]2020

7. Wang J. Numerical simulation of corneal refractive surgery based on improved reconstruction of corneal surface: University of Liverpool; [Doctoral thesis]2015.

8. Eliasy A, Chen KJ, Vinciguerra R, Lopes BT, Abass A, Vinciguerra P, Ambrosio R, Jr., Roberts CJ, Elsheikh A. Determination of Corneal Biomechanical Behavior in-vivo for Healthy Eyes Using CorVis ST Tonometry: Stress-Strain Index. Front Bioe Biot 2019;7:105.

9. Elsheikh A, Geraghty B, Alhasso D, Knappett J, Campanelli M, Rama P. Regional variation in the biomechanical properties of the human sclera. Exp eye res 2010;90(5):624-633.

10. Kotecha A, Elsheikh A, Roberts CR, Zhu H, Garway-Heath DF. Corneal thickness-and age-related biomechanical properties of the cornea measured with the ocular response analyzer. Inv opht vis sci 2006;47(12):5337-5347.

11. Villamarin A, Roy S, Hasballa R, Vardoulis O, Reymond P, Stergiopulos N. 3D simulation of the aqueous flow in the human eye. Med engi phy 2012;34(10):1462-1470.

12. Eliasy, A., Abass, A., Lopes, B.T., Vinciguerra, R., Zhang, H., Vinciguerra, P., Ambrosio Jr, R., Roberts, C.J. and Elsheikh, A., 2020. Characterization of cone size and centre in keratoconic corneas. Journal of the Royal Society Interface, 17(169), p.20200271.

13. Zvietcovich, F., Nair, A., Ambekar, Y.S., Singh, M., Aglyamov, S.R., Twa, M.D. and Larin, K.V., 2020. Confocal air-coupled ultrasonic optical coherence elastography probe for quantitative biomechanics. Optics Letters, 45(23), pp.6567-6570.